On the possible identification of defects using the autocorrelation function approach in double Doppler broadening of annihilation radiation spectroscopy

1998 J. Phys.: Condens. Matter 10 10475

(http://iopscience.iop.org/0953-8984/10/46/015)

J. Phys.: Condens. Matter **10** (1998) 10475–10492. Printed in the UK PII: S0953-8984(98)97623-8

On the possible identification of defects using the autocorrelation function approach in double Doppler broadening of annihilation radiation spectroscopy

C D Beling†, W LiMing†, Y Y Shan†, S H Cheung†, S Fung†, B K Panda‡ and A P Seitsonen§

† Department of Physics, University of Hong Kong, Pokfulam Road, Hong Kong, People's Republic of China

‡ Forschungszentrum Rossendorf, Postfach 510119, D-01314 Dresden, Germany

§ Fritz-Haber-Institute der Max-Plank-Gesellschaft, Faraday 4–6, 14195 Berlin—Dahlem, Germany

Received 30 April 1998

Abstract. The recent revived interest in the use of double-Doppler broadening of annihilation radiation (D-DBAR) spectroscopy, which employs two Ge detectors in back-to-back geometry, has stemmed mainly from its potential in defect identification as a result of its elemental sensitivity through core annihilations in atoms at the defect site. Emphasis has thus largely concentrated on the high momentum spectral range. In contrast the present work emphasizes the need to also focus attention on the low momentum region of the D-DBAR spectra. It is argued that the $\sqrt{2}$ improved resolving power of D-DBAR, in conjunction with spectral deconvolution, should give future 1D (one dimensional) momentum data approaching in quality those obtainable using 1D-ACAR (angular correlation of annihilation radiation), thus forming an alternative technique for observing the structure containing diffraction patterns that originate from annihilations with localized electron states at positron trapping defects. Rotation of the sample about a specified crystal axis, and the binning of events by angle, is suggested as a means of extending the technique to form a 2D- (two dimensional) DBAR counterpart to 2D-ACAR. The advantages of considering the real space positron electron wavefunction product AF (autocorrelation function), obtained by simple manipulation of the D-DBAR data in Fourier space, are outlined. In particular the possible visualization offered in real space of a defect's physical geometry, with the prospect of building up a library of contour patterns for future defect identification, is discussed, taking the silicon monovacancy in Si and the negative As vacancy in GaAs as examples.

1. Introduction

Positrons are well known for their ability to trap into vacancy related defects and to yield information on such defects through the emitted annihilation radiation [1]. Such studies have, in the past, mainly been carried out using single parameter characterization of the positron annihilation data pertaining to the defect. In PAL (positron annihilation lifetime) spectroscopy, for example, information comes from the longer defect related lifetime component in the spectra. In DBAR (Doppler broadened annihilation radiation) spectroscopy the defined S parameter is higher in defects due to more annihilations occurring with low momentum valence electrons [2]. Recent years have, however, seen two important advances in the use of the DBAR technique. The first is the introduction of the dual S

0953-8984/98/4610475+18$19.50

(valence) and W (core) parametrization for a defect, which when displayed in the form of an (S, W) plot against an experimental variable, becomes a powerful way of distinguishing different defects [3]. The second is that of introducing a coincidence detector to reduce background, allowing the technique to become sensitive to core annihilations and thus the chemical environment of the positron within the defect [4].

It is of interest to note that, apart from one earlier study [5], the third main positron annihilation technique, namely ACAR (angular correlation of annihilation radiation) has, in contrast to PAL and DBAR spectroscopies, been almost exclusively reserved for studying Fermi surfaces or valence band structures in defect free materials [6]. Recently, however, there have been some notable departures from this trend. For example Peng *et al* [7] have shown how, using photo-excitation to populate the V_{As}^{-} defect in semi-insulating GaAs, the ACAR spectrum of this defect can be obtained. They suggested that such defect ACAR spectroscopy be used as a means of 'fingerprinting' different defects in materials. Likewise, in a detailed study using both PAL and DBAR spectroscopies to ascertain the relative fractions of V_{As}^{-} and V_{As}^{0} present at different temperatures in n-type GaAs, Ambigapathy *et al* [8] were able to separate out the ACAR spectra for both these charge states of the V_{As} defect. The ACAR spectra showed, as expected, the negatively charged V_{As}^{-} was more inwardly relaxed than V_{As}^{0}.

Recently the subject of defect identification using ACAR has been addressed theoretically by McMullen and Bishop [9] who suggested that the observed ACAR spectrum of a defect should be considered as the diffraction pattern of the defect. This being so, defect-ACAR could be far more than just a convenient defect fingerprinting tool, if, as a diffraction pattern, spectra could through Fourier inversion provide the spectroscopist with some direct visual structure of a crystal defect. In this context, it has been known for some time that the Fourier transformation of the momentum distribution gives in real space the autocorrelation function (AF) of the positron–electron wavefunction product at the site of annihilation [10]. Visual structural information on the crystal lattice can indeed be seen for full-band materials such as semiconductors, where zero passages in the AF occur very close to the Bravais lattice positions, thus giving some kind of lattice image [10–12]. The question, however, as to what perturbation, if any, occurs to the positions of these AF zero passages, if positrons annihilate from a vacancy defect state rather than the Bloch state has not yet been satisfactorily addressed. For example one might naturally speculate as to whether or not, if there is an inward atomic relaxation at the defect site, there might also be a related inward shift of the lattice related positions of the AF zero passages.

Another recent development has been the resurgence of interest in the D- (double) DBAR technique [13] stimulated by the need to gain elemental specificity to atoms at a defect site localizing the positron [4]. The technique employs two Ge detectors that operate in back-to-back configuration so as to detect the energy of both annihilation photons, and gives rise to symmetric spectra with very low background [14]. Although suffering from poorer momentum resolution than its 1D (one dimensional) ACAR counterpart, D-DBAR in fact makes an important complimentary tool, through its ability to access the core electron momentum distributions outside the typical 10^{-2} mc (10 mrad) ACAR working range [14]. As regards the poorer resolution, D-DBAR does have the advantage over conventional DBAR spectroscopy in that a $\sqrt{2}$ ($\sim$40%) improvement in instrumental resolution is obtained as a result of the individual errors from each Ge detector adding in quadrature [2]. Capitalizing on this fact and employing deconvolution software, Britton *et al* [15] built a D-DBAR system with a 386 eV effective resolution (fwhm) (1.5 mrad ACAR equivalent). They also speculated that further improvements could make D-DBAR of competitive resolving power to ACAR spectrometers (fwhm $\sim$ 0.5–1 mrad) [15]. This

being the case, D-DBAR would have a significant advantage over 1D-ACAR, namely that of a significantly higher efficiency. Essentially the same quality of spectrum could be obtained but with a much reduced source activity making the D-DBAR spectrometer a versatile instrument for studying defect valence structures in the low momentum regime, while still retaining the advantage of being able to inspect the high momentum (core electron) regime.

The purpose of this paper is twofold. First, using a theoretical approach and within the context of 2D-ACAR spectroscopy, we attempt to show the potential of forming a 2D-AF mapping for aiding atomic structural identification of crystal defects. Second, by discussing experimental aspects, our aim is to demonstrate that D-DBAR spectroscopy (and its 2D extension, 2D-DBAR spectroscopy) has the potential to form an essentially equivalent tool for defect identification. The structure of this paper is as follows. In section 2 we review the idea of the 2D-ACAR spectrum of defect trapped positrons as being the diffraction pattern of the defect [9]. Here, for purposes of aiding the discussion, the momentum distributions pertaining to the V_{As}^{-} defect in GaAs as presented in [9] are repeated. In section 3 of the paper the AF formalism is reviewed, the point being stressed that the 2D (two dimensional) AF mapping is probably the best real space structural view that quantum mechanics allows of the crystal defect. AF mappings obtained from the simple tetrahedrally coordinated defect model of [9] are compared with results obtained from the relaxed state of the V_{Si}^{0} in Si obtained using an *ab initio* pseudopotential supercell calculation. In section 4 of the paper attention is turned to D-DBAR spectroscopy, where arguments are given showing that the technique has both the potential of approaching ACAR spectroscopy in terms of resolving power, and a natural connection with AF mapping formalism. A 2D (two dimensional) form of DBAR momentum spectroscopy is considered which involves rotation of the sample between the two detectors. Conclusions are drawn in section 5. Throughout we reserve the nomenclature D-DBAR for the essentially 1D momentum spectroscopy produced by dual parameter system of Ge detectors, and the term 2D-DBAR is strictly confined to the analogue of 2D-ACAR, namely the measurement of the 2D projection of 2γ momentum space.

2. The defect diffraction pattern

Here, as a means of aiding discussion we follow closely the ideas of McMullen and Bishop who recently pointed out that the momentum distribution of 2γ annihilation photon pairs arising from annihilations with localized defect electron orbitals form what in reality is a diffraction pattern of the defect [9]. They considered the case of a positron localized at a V_{As}^{-} vacancy defect in GaAs, and its subsequent annihilation with the four dangling bond localized electron states that hybridize into a_1 and t_2 states [16]. The probability density in 2γ momentum space $\rho^{2\gamma}(\boldsymbol{p})$, neglecting any enhancement effects, is thus given as a summation over these four localized electron states of the diffraction type integrals:

$$\begin{aligned}\rho^{2\gamma}(\boldsymbol{p}) &= \sum_{j=1}^{4}\left|\int \varphi_{+}(r)\psi_j(r)\,\mathrm{e}^{\mathrm{i}\boldsymbol{k}\cdot\boldsymbol{r}}\,\mathrm{d}^3r\right|^2 \\ &= \sum_{j=1}^{4}\sum_{i=1}^{4} a_{ij}\left|\int \varphi_{+}(r)\varphi_i(r)\,\mathrm{e}^{\mathrm{i}\boldsymbol{k}\cdot\boldsymbol{r}}\,\mathrm{d}^3r\right|^2 \qquad (1)\end{aligned}$$

where the first summation is over the four electron states, the second is over the four nearest neighbour atoms and the a_{ij} are the linear coefficients of the ith dangling atomic orbital to the total electron wavefunctions ψ_j. For the V_{As}^{-} defect (and its analogue V_{Si}^{0}) the summation in (1) breaks into two, the first being for the two electrons in the a_1 state, and the second

the two in the t_2 state. As pointed out in [9] the diffraction-like nature of $\rho^{2\gamma}(\boldsymbol{p})$ is made clearer by recognizing that the jth positron–electron wavefunction product $\varphi_+(r)\varphi_j(r)$ is a function peaked at some position $\beta\boldsymbol{R}_i$ ($\boldsymbol{R}_i$ being the ith atom's position) due to both the falling-off in the positron wavefunction and the rising of the electron wavefunction. The form of (1) may thus be rewritten in the more transparent form [9]:

$$\rho^{2\gamma}(\boldsymbol{p}) \approx \sum_{j=1}^{4} \left| \sum_{i=1}^{4} a_{ij} \exp(\mathrm{i}\boldsymbol{k}\cdot\beta\boldsymbol{R}_i) \right|^2 = \sum_{j=1}^{4} \rho_j^{2\gamma}(\boldsymbol{p}) \tag{2}$$

where one notes that for a single electron state j, $\rho_j^{2\gamma}(\boldsymbol{p})$ is a diffraction pattern with phasing between the four atomic wave components coming both from the a_{ij} (essentially aperture functions) and the phase factors $\exp(\mathrm{i}\boldsymbol{k}\cdot\beta\boldsymbol{R}_i)$. Maxima occur in $\rho_j^{2\gamma}(\boldsymbol{p})$, under constructive interference conditions when an integral number of Compton wavelengths (h/mc) fit along the path length difference between any two positron–atomic distances $\beta\boldsymbol{R}_i$ in the direction of observation, assuming a_{ij} to be of the same sign for both atoms. With the Compton wavelength being 0.024 Å and typical interatomic distances $\sim$5 Å diffraction maxima are expected at $\sim 10^{-3}$ mc momenta, and are just within range of high resolution ACAR spectrometers.

We follow further the procedure of [9] treating the positron wavefunction simply as a single Gaussian function centred at the origin:

$$\varphi_+(\boldsymbol{r}) = \frac{\alpha_0}{\sqrt{\pi}}\, \mathrm{e}^{-\alpha_0^2 r^2} \tag{3}$$

while the localized electron states are approximated by hybrids of the four dangling atomic orbitals (also taken as Gaussians) of the nearest tetrahedrally coordinated neighbour atoms [16]:

$$\psi_j(\boldsymbol{r}) = \sum_{i=1}^{4} a_{ji}\varphi_j(\boldsymbol{r}) = \frac{\alpha}{\sqrt{\pi}} \sum_{i=1}^{4} a_{ji}\, \mathrm{e}^{-\alpha^2(\boldsymbol{r}-\boldsymbol{R}_i)^2} \tag{4}$$

where the two lowest energy a_1 states (within the valence band) have

$$a_{j1} = a_{j2} = a_{j3} = a_{j4} = 1 \tag{5}$$

and the two higher energy t_2 states (within the bandgap) have

$$a_{j1} = a_{j4} = 1 \qquad a_{j2} = a_{j3} = -1. \tag{6}$$

This model permits an analytical form for the three dimensional $\rho^{2\gamma}(\boldsymbol{p})$ distribution for the a_1 and t_2 states as given by equations (5) and (6) of [9]. Single integration over p_z, the [001] direction, gives the expected 2D-ACAR spectra $N(p_x, p_y)$:

$$N(p_x, p_y) = \int_{p_z} \rho^{2\gamma}(\boldsymbol{p})\, \mathrm{d}p_z. \tag{7}$$

The a_1 and t_2 states both give rise to different $N(p_x, p_y)$ and these are shown in figures 1(a) and 1(b) respectively. These spectra show the diffraction-like features expected from a tetrahedrally coordinated structure, with the same minima occurring at 6.3 mrad in the [100] and [010] crystallographic directions as reported in [9]. Diffraction maxima are seen along the [110] and [$\bar{1}$10] directions for both a_1 and t_2 states as expected since the projections of the four atoms onto the (001) plane lie along these directions. The summed diffraction pattern over all four electron states is thus of the same basic form as in figure 1, although the more t states are present (for example in going from V_{As}^0 to V_{As}^-) the more sharp the diffraction minima and maxima become.

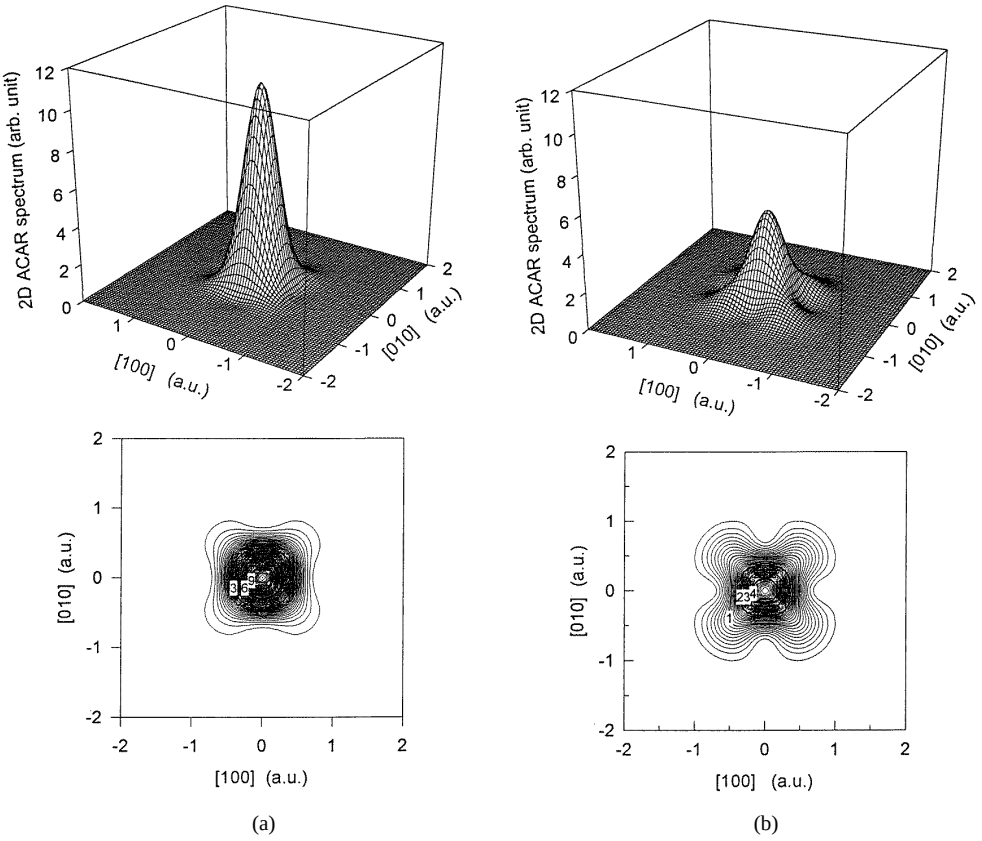

Figure 1. 2D-ACAR, $N(p_x, p_y)$, relief plots (upper diagram) and contour plots (lower diagram) for V_{As}^{-} trapped positrons annihilating with (a) the a_1 state orbitals and (b) the t_2 state orbitals according to the model of McMullen and Bishop [9].

The understanding of why one expects to see diffraction patterns from positron trapped at defects [9], and the available experimental support for such patterns [7, 8] suggest this to be a useful line of research into the atomic microstructure of crystal defects. However, it is apparent that there are some difficulties hindering progress in this direction. The first is seen in equations (1) and (2), which show us that experimentally one observes not just the diffraction pattern from one localized electron state, but indeed a sum over all the localized states. This makes it difficult to separate the individual states, and thereby to obtain accurate structural information. Secondly, we believe, and will endeavour to show in the following section, that equation (1) embodies only a partial picture in that the positron wavefunction overlaps not just with the localized dangling bond electrons, but also with the de-localized valence Bloch states of neighbouring atoms. The consequence is that there will be a high background signal associated with the de-localized states against which the diffraction signal from the localized states must be separated. One way of overcoming such difficulties is to perform 'difference' spectra experiments which isolate the diffraction pattern from just a single electron state. For example one can chop from 'light-on' conditions (in which case a specific localized electron state is populated) and 'light-off' conditions (when the same localized state has zero occupancy) [4]. Alternatively, by studying defects within the depletion region of a semiconductor junction, one should be able to populate defects

associated deep levels by an electrical filling pulse, and then to distinguish the annihilation radiation from the different charge states of mid-gap electronic defects according to their characteristic thermal emission rates [17].

3. The autocorrelation function approach to defect identification

An alternative, but complimentary way of dealing with the defect structural information present in the annihilation radiation is that of working with the autocorrelation function (AF) of the positron–electron wavefunction product $\psi_{+,j}(\boldsymbol{r}) = \varphi_{+}(\boldsymbol{r})\psi_j(\boldsymbol{r})$, expressed as [10]

$$B_j^{2\gamma}(\boldsymbol{r}) = \int \psi_{+,j}^{*}(\boldsymbol{r}+\boldsymbol{s})\psi_{+,j}(\boldsymbol{s})\,\mathrm{d}^3 s. \tag{8}$$

This function is simply the Fourier transform of the observed momentum density $\rho^{2\gamma}(\boldsymbol{p})$:

$$B^{2\gamma}(\boldsymbol{r}) = \int \rho^{2\gamma}(\boldsymbol{k})\exp(\mathrm{i}\boldsymbol{k}\cdot\boldsymbol{r})\,\mathrm{d}^3 k = \sum_j \int \rho_j^{2\gamma}(\boldsymbol{k})\exp(\mathrm{i}\boldsymbol{k}\cdot\boldsymbol{r})\,\mathrm{d}^3\boldsymbol{k} = \sum_j B_j^{2\gamma}(\boldsymbol{r}) \tag{9}$$

a fact that results simply from the Wiener and Khintchine theorem, which states that the Fourier transform of a function's autocorrelogram (i.e. $B_j^{2\gamma}(\boldsymbol{r})$) is the power spectrum of the function (i.e. $\rho_j^{2\gamma}(\boldsymbol{p})$) [18]. The main use of $B^{2\gamma}(\boldsymbol{r})$ has in the past been in reconstructing full three-dimensional momentum densities $\rho^{2\gamma}(\boldsymbol{p})$ for perfect (non-defected) crystals from the one and two dimensional projections that DBAR and ACAR spectroscopies provide [19, 20]. The point emphasized here is that, with regard to positron annihilation radiation originating from vacancy traps, $B^{2\gamma}(\boldsymbol{r})$ also presents itself as a function with useful application, being probably the best real-space visualization of the defect's atomic structure that quantum mechanics will allow.

From the diffraction-like nature of equation (1) the first thought is that, as in the case of coherent scattering, one has only to take the square root of the observed momentum density, infer a sign, and carry out an inverse Fourier transformation in order to retrieve the positron–electron wavefunction product (which takes on the role of a kind of aperture function). This is, of course, not permissible since all phase information pertaining to the wavefunction is lost in the process of measurement [21]. This problem appears intractable, and although future ways of grafting in phase information, perhaps using symmetry arguments, may be found, it seems that direct Fourier transformation is the only route available without making additional inferences or assumptions. Moreover, it seems this is a route worthy of pursuit because, although an exact real-space image is not obtained, the defect's spatial structure should still be quite apparent and deducible from an autocorrelation map through the form of equation (8). We proceed to check the validity of this suggestion by considering first the case of the V_{As}^{-} vacancy in GaAs using the more transparent analytical dangling bond model of McMullen and Bishop [9] as outlined in section 1.

The combined a_1 and t_2 autocorrelation functions $B^{2\gamma}(x, y)$ as obtained under Fourier transformation of the 2D-ACAR patterns are shown in figures 2(a) and 2(b) respectively. One notes that peaks (or rather protruding 'feet' since they are not fully resolvable) occur along the [110] and [$\bar{1}$10] directions, which are directions in which the four neighbour atoms project onto the (001) plane. This is as expected, seeing that for both a_1 and t_2 states, shifting $\psi_{+,j}(\boldsymbol{r})$ along the [110] and [$\bar{1}$10] directions causes an autocorrelation, as expressed by equation (8), at the atomic separations along these directions (i.e. at $a/\sqrt{2} = 7.55$ au) assuming incorrectly the maximum of $\psi_{+,j}(\boldsymbol{r})$ at $\boldsymbol{r} = \boldsymbol{R}_i$. Due to the convolution of the

positron and electron wavefunctions $\psi_{+,j}(\boldsymbol{r})$ in fact maximizes at the attenuated interatomic distance of $\alpha^2/(\alpha^2+\alpha_0^2)(a/\sqrt{2}) = 5.13$ au, which on observation of the $B^{2\gamma}(x, y)$ are the locations of the centres of the 'feet'. A most obvious and yet important feature of these $B^{2\gamma}(x, y)$ mappings is the way in which after a certain radial distance the autocorrelation function approaches zero. The reason is obvious because on the McMullen and Bishop model the positron only interacts with its nearest neighbour atoms, in which case once one interatomic distance has been traversed, the wavefunction autocorrelation can only drop to zero. A corollary to this is that if it becomes experimentally feasible to measure the autocorrelation function sufficiently far out from the origin, then the disappearance of the $B^{2\gamma}(\boldsymbol{r})$ signal would be a clear indication of saturation vacancy trapping. The truth of this statement and in particular the meaning of 'sufficiently far out' will depend in practice on the degree of positron localization in the vacancy, a point that is discussed further below.

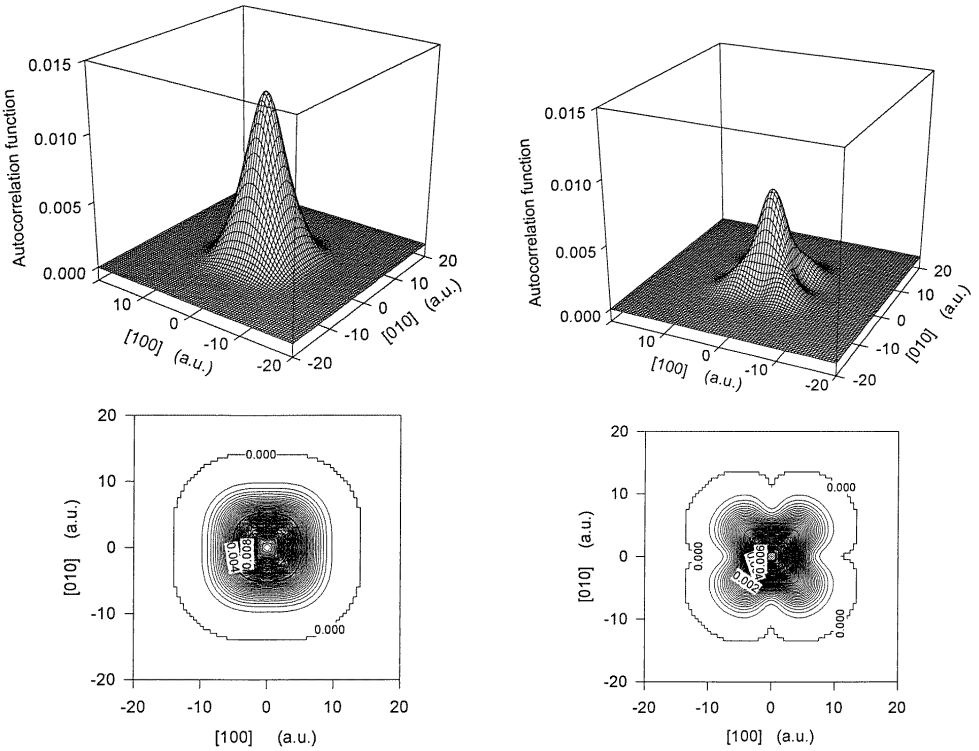

Figure 2. (001) plane 2D-AF (autocorrelation function), $B^{2\gamma}(x, y)$, relief plots (upper diagram) and contour plots (lower diagram) for V_{As}^{-} trapped positrons annihilating with (a) the a_1 state orbitals and (b) the t_2 state orbitals according to the model of McMullen and Bishop [9]. The crosses mark the positron attenuated nearest neighbour interatomic separation as projected onto the (001) plane.

To investigate the autocorrelation function of a vacancy trapped positron further we have performed *ab initio* first-principles pseudopotential calculations on the valence band structure in bulk Si and the V_{Si}^0 defect using the computer code FHI96MD of Stumpf and Scheffler [22]. The pseudopotentials employed were of the fully separable norm-conserving Bachelet–Hamann–Schlüter type [23, 24]. In the case of the V_{Si}^0 defect, modelling was by

way of a $2 \times 2 \times 2$ supercell (i.e. with 16 atoms) in the fcc basis. The plane wave expansion coefficients $C_{nk}(\boldsymbol{G})$ of the of the electron wavefunctions were computed up to a cutoff of 30 Ryd for the six special k points of Chadi and Cohen [25]. However, to correctly symmetrize the AF and the electron charge density, the symmetric mapping points of the six special k points in the summation over k space have to be included. The wavefunctions at each of these 80 points are given by:

$$C_{n,\hat{g}\boldsymbol{k}_i}(\boldsymbol{G}) = \sum_{\boldsymbol{G}'} C_{n\boldsymbol{k}_i}(\boldsymbol{G}')\delta_{\boldsymbol{G},\hat{g}\boldsymbol{G}'} \tag{10}$$

where the $\boldsymbol{k}_i$ are the Chadi–Cohen special points and $\hat{g}$ is a group element belonging to the symmetry group T_d.

In order to calculate the positron wavefunction using density functional theory, the electron density $\rho(\boldsymbol{r})$ is required and was computed as

$$\rho(\boldsymbol{r}) = 2\sum_{n}\sum_{\hat{g}}^{T_d}\sum_{\boldsymbol{k}_i}^{6}\sum_{\boldsymbol{G}} e^{i\boldsymbol{G}\cdot\boldsymbol{r}} \sum_{\boldsymbol{G}'} C_{n,\hat{g}\boldsymbol{k}}(\boldsymbol{G}')C_{n,\hat{g}\boldsymbol{k}}(\boldsymbol{G}-\boldsymbol{G}') \tag{11}$$

where the sum over the group T_d includes only those elements which generate $\hat{g}\boldsymbol{k}_i \neq \boldsymbol{k}_i$. The positron wavefunction expansion coefficients $A(\boldsymbol{G})$ were then obtained by diagonalizing the positron Hamiltonian in reciprocal lattice space with the potential:

$$V_+(\boldsymbol{G}) = \frac{4\pi e^2 Z_v}{\boldsymbol{G}^2\Omega} - \frac{4\pi e^2}{\Omega}\rho(\boldsymbol{G}) + V_{Corr}^{BN}(\boldsymbol{G}) \tag{12}$$

where the first, second and third terms are the ion core, Hartree and positron–electron correlation terms respectively. $\rho(\boldsymbol{G})$ and are $V_{Corr}^{BN}(\boldsymbol{G})$ respectively the Fourier transforms of $\rho(\boldsymbol{r})$ and the Boronski and Nieminen parametrization of the electron–positron correlation potential [26]. The Fourier components of the combined positron–electron wavefunction $D_{nk}(\boldsymbol{G})$ are finally obtained through the convolution:

$$D_{n,\hat{g}\boldsymbol{k}_i}(\boldsymbol{G}) = \sum_{\boldsymbol{G}'} C_{n,\hat{g}\boldsymbol{k}_i}(\boldsymbol{G}')A(\boldsymbol{G}-\boldsymbol{G}') \tag{13}$$

which are then used to compute $B^{2\gamma}(\boldsymbol{r})$ according to [27]:

$$B^{2\gamma}(\boldsymbol{r}) = \frac{1}{\Omega}\sum_{n}\sum_{\hat{g}}^{T_d}\sum_{\boldsymbol{k}_i}^{6} e^{ig\boldsymbol{k}_i\cdot\boldsymbol{r}} \sum_{\boldsymbol{G}} |D_{n,\hat{g}\boldsymbol{k}}(\boldsymbol{G})|^2 \exp(i\boldsymbol{G}\cdot\boldsymbol{r}) \tag{14}$$

from which either $B^{2\gamma}(x, y)$ or $B^{2\gamma}(z)$ can be obtained by making $\boldsymbol{r}$ a vector in either in the x, y plane or along the z direction respectively.

In figures 3(a) and 3(b) we show the two dimensional autocorrelation functions $B^{2\gamma}(\boldsymbol{r})$ on the (001) plane for the bulk $|B\rangle$ and defect $|D\rangle$ states respectively. It is seen that $B^{2\gamma}_{|B\rangle}(\boldsymbol{r})$ possesses the interesting and well recognized property of becoming zero at the Bravais lattice positions $\boldsymbol{r} = \boldsymbol{R}$ [10, 21]. This result, which is essentially a manifestation of the delocalization of the positron wavefunction over the whole crystal lattice, derives simply from equation (14), since:

$$B^{2\gamma}(\boldsymbol{R}) = \frac{1}{\Omega}\sum_{n\boldsymbol{k}} e^{i\boldsymbol{k}\cdot\boldsymbol{R}} \sum_{\boldsymbol{G}} |D_{n\boldsymbol{k}}(\boldsymbol{G})|^2 \approx \frac{1}{\Omega}\sum_{n\boldsymbol{k}} e^{i\boldsymbol{k}\cdot\boldsymbol{R}} = \delta_{\boldsymbol{R},0}. \tag{15}$$

The approximation in equation (15), that is absent in Compton profile spectroscopy [21], arises because of the convolution of the positron component into the positron–electron product wavefunction (equation (13)). The positron–electron enhancement factor, not included in equation (15), also has an effect on the positions of the zero passages, but

one which is considerably weaker [12, 28]. In semiconductors both effects cause the zero passages to be shifted slightly radially outwards by ∼0.4 au (5% of the inter-atomic separation) in semiconductors [11, 12, 28]. In the present case this outwards shift may be seen clearly from figure 4 which shows the variation of $B^{2\gamma}(\boldsymbol{r})$ along the [110] direction. For the Bravais displacement $\boldsymbol{R}_{11}$ in Si (lattice constant = 10.2 au) the expectation would be a zero passage at 7.26 au, and yet the calculated position (excluding enhancement) is shifted outwards by 0.25 au.

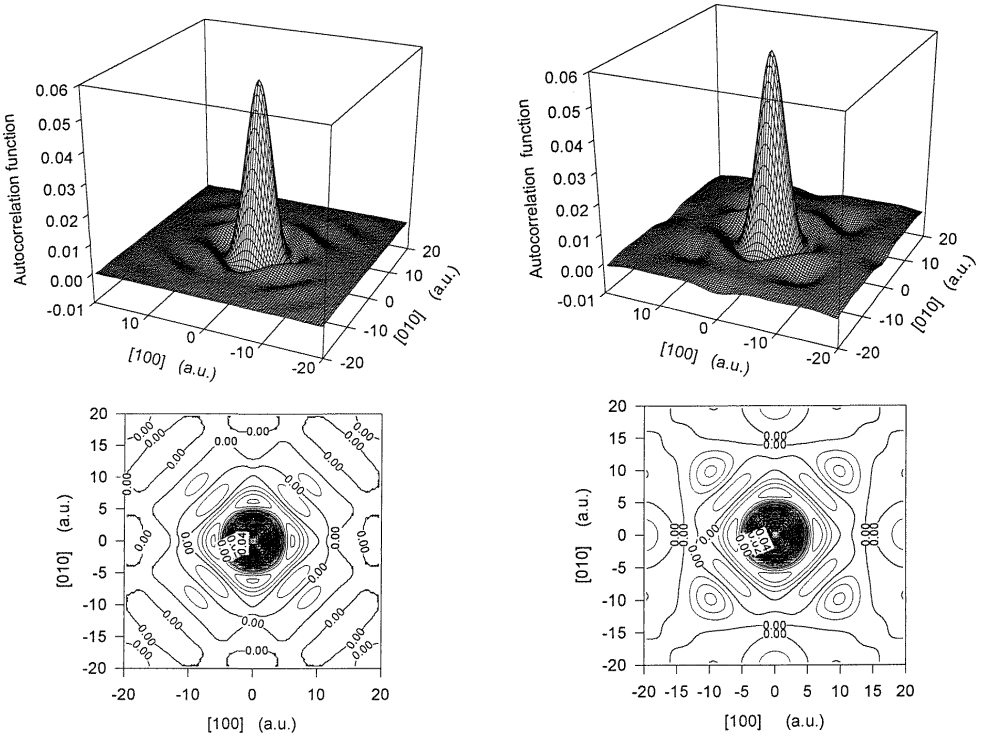

Figure 3. (001) plane 2D-AF (autocorrelation function). The figure shows $B^{2\gamma}(x, y)$ relief plots (upper diagram) and contour plots (lower diagram) for (a) delocalized Bloch state positrons in Si and (b) V_{Si}^{0} trapped positrons in Si. The dips at ±20 au positions along the [100] and [010] directions are artifacts caused by the limited supercell size.

The long range 'rippling' effect occurring predominantly along [110] and $[\bar{1}10]$ as seen in figure 3(a) has some common origin with the 'feet' that occur in these directions for the $|D\rangle$ state as discussed above, and as shown in figure 2: namely that it is in these directions that the electron wavefunctions are localized on atomic sites. That is the overlapping of the displaced wavefunction $\psi_{+,j}(\boldsymbol{r}+\boldsymbol{s})$ in these directions will naturally lead to maximal overlap with $\psi_{+,j}(\boldsymbol{r})$ when $\boldsymbol{s}$ equates with an integer number of inter-atomic separations. The fact that, as seen in figures 3(a) and 4, $B^{2\gamma}_{|B\rangle}(\boldsymbol{r})$ is zero rather than maximum when $\boldsymbol{r} = n\boldsymbol{R}_{110}$ results because of interference between the full complement of valence band k states (equation (15)) [21]. In spite of this effective $\pi/2$ radial outwards phase shift in the AF plot, the property of maximum autocorrelation along the directions in which atoms are situated is still retained, providing both a helpful visualization of the lattice and a means of

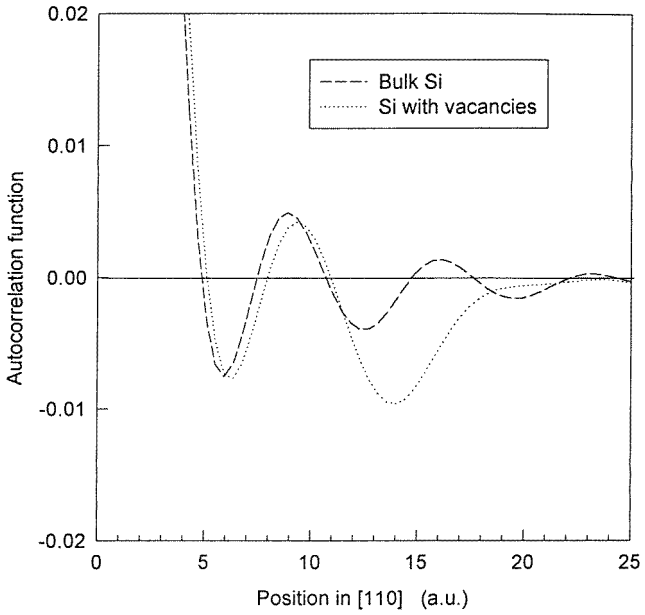

Figure 4. [110] direction 1D-AF (autocorrelation function), for Si bulk delocalized positrons and V_{Si}^0 trapped positrons in Si, according to the *ab initio* pseudopotential calculation described in the text.

checking the degree of positron non-localization in a crystal.

Turning attention now towards the defect trapped positron state, we see that its AF mapping $B_{|D\rangle}^{2\gamma}(\boldsymbol{r})$, as shown in figure 3(b) and 4, clearly shows differences from $B_{|B\rangle}^{2\gamma}(\boldsymbol{r})$. It is noted that:

(i) the autocorrelation reduces to zero for $|\boldsymbol{r}| > 18$ au;

(ii) the autocorrelation extends approximately twice as far as predicted by [9] (figure 2);

(iii) the correlation with atomic positions is $B_{|B\rangle}^{2\gamma}(\boldsymbol{r})$-like only to nearest neighbour sites and

(iv) the positions of zero passage in the [110] direction are shifted outwards (figure 4).

Points (i) and (ii) may be simply understood in terms of the structure of the positron density $|\varphi_+(\boldsymbol{r})|^2$ around the defect site. This is shown in figure 5. It is noted that the positron does not only overlap with the nearest atoms, but that it extends out into the interstitial regions of the next atomic shell [8]. The positron localization explains point (i) while the point (ii) results from the localization not being as confined as modelled in [9] with the positron sensing the environment out to the next coordination layer of defect atoms.

The explanation of points (iii) and (iv) is not so obvious. We note though, that if the positron was just annihilating with localized electron orbitals as suggested in [9], it would follow that a peak (i.e. one of the 'feet' in figure 2) should occur at around 7.26 au in the 1D AF plot (figure 4). Instead we see a $B_{|B\rangle}^{2\gamma}(\boldsymbol{r})$-like summed k-space interference effect at this position reducing $B_{|D\rangle}^{2\gamma}(\boldsymbol{r})$ to a slightly negative value. The suggestion is that a large fraction of positrons are annihilating with de-localized electrons on the nearest neighbour atoms. This is not unexpected. Only one electron out of the four valence electrons belonging to each neighbouring Si atom contributes to the localized a_1 and t_2 orbital leaving three in normal

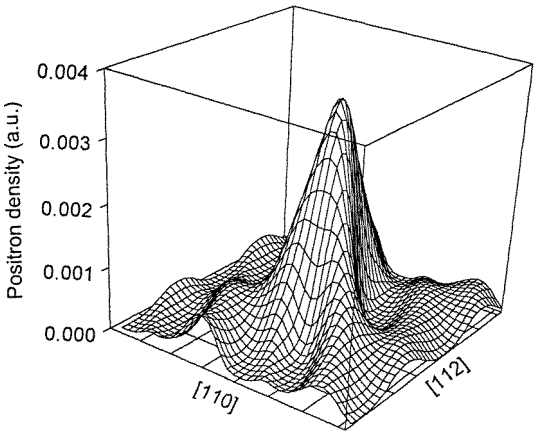

Figure 5. Relief plot of the positron density in the $(1\bar{1}0)$ plane according to the *ab initio* pseudopotential calculation described in the text. The dips correspond to the locations of Si atoms.

valence bonding states. Statistically, assuming equal weighting, one would therefore expect 75% of the positron signal to originate from de-localized valence electrons. In practice one might expect a smaller percentage seeing that the localized electron orbitals formed from dangling bonds are inward directed [16]. Although we do not fully understand as yet the outward shifts in zero passage positions (i.e. point (iv)), the suggestion is that the effect results from the combined removal of certain delocalized electron states and introduction of localized ones. We also note that our calculation gives a $\sim$4% inward relaxation or the nearest neighbour atom positions, and that this is also likely to have a significant effect on the zero passage positions.

The above study strongly suggests that there is a good deal of annihilation signal coming from delocalized electrons at the vacancy site. This being so one may write the 3D momentum density originating from the defect state as:

$$\rho_{def}^{2\gamma}(\boldsymbol{p}) = \sum_{j=1}^{nloc} \left| \int \varphi_{+}^{loc}(\boldsymbol{r}) \psi_{j}^{loc}(\boldsymbol{r})\, \mathrm{e}^{\mathrm{i}\boldsymbol{k}\cdot\boldsymbol{r}}\, \mathrm{d}^3 r \right|^2 + \sum_{j>nloc} \left| \int \varphi_{+}^{loc}(\boldsymbol{r}) \psi_{j}^{val}(\boldsymbol{r})\, \mathrm{e}^{\mathrm{i}\boldsymbol{k}\cdot\boldsymbol{r}}\, \mathrm{d}^3 r \right|^2 \tag{16}$$

where the first summation originates from annihilations with a number $nloc$ localized electron orbitals, and the second from the remaining full complement of valence band Bloch states. Equation (16) may also be re-expressed in the form:

$$\rho_{def}^{2\gamma}(\boldsymbol{p}) = \eta \rho_{loc}^{2\gamma}(\boldsymbol{p}) + (1-\eta)\rho_{val}^{2\gamma}(\boldsymbol{p}) \tag{17}$$

where η is the fraction of positrons that annihilate with localized defect electron orbitals and $\rho_{loc}^{2\gamma}(\boldsymbol{p})$ and $\rho_{val}^{2\gamma}(\boldsymbol{p})$ are respectively the 3D momentum densities from the localized and delocalized electron states. A similar expression follows simply for the autocorrelation function:

$$B_{def}^{2\gamma}(\boldsymbol{r}) = \eta B_{loc}^{2\gamma}(\boldsymbol{r}) + (1-\eta) B_{val}^{2\gamma}(\boldsymbol{r}) \tag{18}$$

with $B_{loc}^{2\gamma}(\boldsymbol{r})$ and $B_{val}^{2\gamma}(\boldsymbol{r})$ being the respective AFs from the localized and delocalized electron states sensed by the positron in its defect trapped state.

The suggestion that the positron annihilates appreciably with non-localized electrons which contain little structural information by way of the defect's diffraction presents the

experimentalist with a problem. As pointed out in section 2 the forms of equations (17) and (18) suggest the need to carry out 'difference in electron occupancy' experiments in looking clearly at defect structures [7, 17]. The alternative scenario is that, should further studies show that $B^{2\gamma}_{val}(\boldsymbol{r})$ is close in form to $B^{2\gamma}_{|B\rangle}(\boldsymbol{r})$ then equation (18) would possibly allow the fraction η to be determined and thereby an experimental isolation of the more useful $B^{2\gamma}_{loc}(\boldsymbol{r})$ function.

4. Towards high resolution D-DBAR and 2D-DBAR spectra

The aim of this section is to first give convincing evidence that D-DBAR spectroscopy may in future, with due care being taken, compete with its 1D-ACAR counterpart in terms of momentum resolution. Based on this we then indicate how a true 2D-DBAR system of resolution approaching the 2D-ACAR counterpart may be established. Finally, within the context of general positron–electron momentum spectroscopy (DBAR or ACAR), we consider the possible spatial viewing range of an experimental AF plot, and thereby demonstrate the need for high resolution spectroscopy systems if such plots are to be helpful in defect structural determination.

As pointed out by MacKensie [2] and demonstrated by Lynn *et al* [14] the combining of the Doppler shifted spectra from two Ge detectors effectively reduces the instrumental resolution by at least a factor of $\sqrt{2}$. This arises as a result of the difference signal between detector outputs being doubled, the blue shift on one photon essentially adding to the red shift on the other, while the instrumental errors from each detector are uncorrelated and add only in quadrature. Britton *et al* [15] were able to achieve a resolution of 840 eV (full width at half maximum) using two standard Ge detectors, corresponding to an ACAR resolution of 3.3 mrad. With the recent advent of digital signal processing in Ge detector technology the prospects look good for even better performance in the future. Resolution improvements of 10 to 20% have recently been noted by one manufacturer using this new technology [29].

Since dramatic improvements in the resolution performance of gamma ray spectroscopy systems are unlikely in the foreseeable future it is necessary to look towards some deconvolution procedure for further significant gains [15]. Such deconvolution is made possible by the fact that there are convenient gamma ray lines such as ^{103}Ru (497 keV), ^{106}Ru (511.8 keV) and ^{85}Sr (514 keV) sufficiently close to the 511 keV annihilation radiation that they effectively give the instrumental response of the system [30, 31]. The fact that the gamma radiation from these sources is uncorrelated presents no real problem since the system can be operated in pseudo-coincidence mode by opening the time coincidence window [14]. In the present work we refer to the response of the hardware (detector + amplifiers + ADCs etc) to a delta function (gamma-ray) input as the hardware instrumental function (HIF) of the system, so as to distinguish it from the equivalent response of the whole instrument (combined hardware + deconvolution software) which is referred to as the residual instrumental function (RIF) [32]. The RIF is simply obtained by deconvoluting the HIF, which in practice amounts to measuring the spectrum of a delta function using the whole hardware+software measurement system. The fwhm (full width at half maximum) resolution of the RIF now becomes the important parameter in addressing the question of how much improvement in resolution can be achieved in deconvoluting D-DBAR spectra. Since, however, the fwhm of the HIF may vary from one D-DBAR

system to another we define here a deconvolution improvement factor F:

$$F = \frac{\text{fwhm(HIF)}}{\text{fwhm(RIF)}}. \tag{19}$$

The procedure of assessing the value of F and its dependence on experimental parameters was to construct an MC (Monte Carlo) computer simulation of the experiment. It was assumed that the shape of the HIF would be close to Gaussian and that any small departures from this form will not cause any serious error. The fwhm of the Gaussian was then taken as being covered by N_{chn} discretizations (experimental channels) (N_{chs} = 6.25, 25, 100, 400, 1600) and the full HIF spectra was taken to have $10N_{chn}$ channels. With a typical fwhm(HIF) being ∼1000 eV this variation corresponds to different energy calibrations (∼0.63, 2.5, 10, 40 and 160 eV/channel) which are essentially the experimentally selectable spectral 'sampling rates'. Experimental D-DBAR spectra were simulated by throwing events into the chosen energy bins using a tested MC (Monte Carlo) code [32]. This event number, i.e. the total spectral counts, N_{cts}, was varied from 10^5 up to 10^8 and represents the second experimentally adjustable parameter. For each N_{chn}, N_{cts} setting, five HIF spectra were obtained and subjected to Fourier transformation. The Fourier coefficients were compared with those of a perfect Gaussian as shown in figure 6 for the case of $N_{chn} = 100$. The departure from the correct Gaussian coefficient marks the cut-off frequency ν_0 on the Stokes–Fourier deconvolution method [31, 34]. While better methods of deconvolution are now available [31, 35–37], we utilize the Stokes method here out of convenience since the RIF takes the simple analytic form $\sin[2\pi\nu_0(\varepsilon/E)]/(\varepsilon/E)$, from which the result $\text{fwhm(RIF)} = (0.603/\nu_0)E$ is obtained, ε being the energy (or momentum or channel) coordinate and E the total spectrum energy (or momentum or channel) range. It is believed that, although in adopting this approach a lower limit on F is obtained, better values may be obtainable though superior deconvolution procedures, the general trend in F will nevertheless be correct. To be systematic in finding a value for ν_0, in view of the statistical scatter seen in figure 6, we first took the mean Fourier coefficient value for frequencies well above ν_0 and then intersected the pure Gaussian coefficient curve at this value. The results obtained for F are shown in figure 7, and suggest the following dependence on N_{chn} and N_{cts}:

$$F = 1.5 + 0.067\ln(N_{cts}N_{chs}). \tag{20}$$

Let us now perform an optimum estimate of system resolution that may be possible. It is conceivable that with source gating on a positron beam, i.e. the 'gating off' of positrons while the detectors are busy processing an annihilation event [38], a total 511 keV peak D-DBAR throughput of 10^4 s^{-1} may be achievable, suggesting that over the period of one day ∼10^9 events may be recorded in a D-DBAR spectrum. With a modern nuclear ADC (analogue to digital converter) digitizing into 16 k channels, operating on a low momentum portion of the spectrum (expanded by means of a biased amplifier), say $|\varepsilon| < 2.6$ keV (|momentum| < 10 mrad) and a HIF of fwhm = 800 eV one obtains $F = 3.4$ and a RIF of fwhm = 230 eV (<1 mrad). The above analysis takes no account of possible improvements with better deconvolution schemes [31, 35–37], but, on the other hand, it also takes no account of the degradation of HIF resolution as count rates are increased to improve the statistics [29]. Much, therefore, remains in the realm of speculation, but the indication is that D-DBAR resolutions approaching those of ACAR spectrometers may be achieved in the foreseeable future.

An important factor to consider in any DBAR spectroscopy system is the problem of amplifier drift. This is unlikely to present any problem, however, if software stabilizes the spectrum, by binning say 100 s accumulations of data into 'mini-spectra' (over which

time amplifier drift should be negligible) and then making a suitable correction to the data according to any noted centroid shift [39]. The result of this procedure is the convolution of a small Gaussian of width $\sim$ fwhm(HIF)/$\sqrt{N_{cts}}$ (i.e. the accuracy with which one can compute the centroid) onto the data. Again working at a 511 keV event rate of 10^4 s^{-1} one has $N_{cts} = 10^6$ and a convolution of $\sim$1 eV which should present little problem as far as deconvolution is concerned.

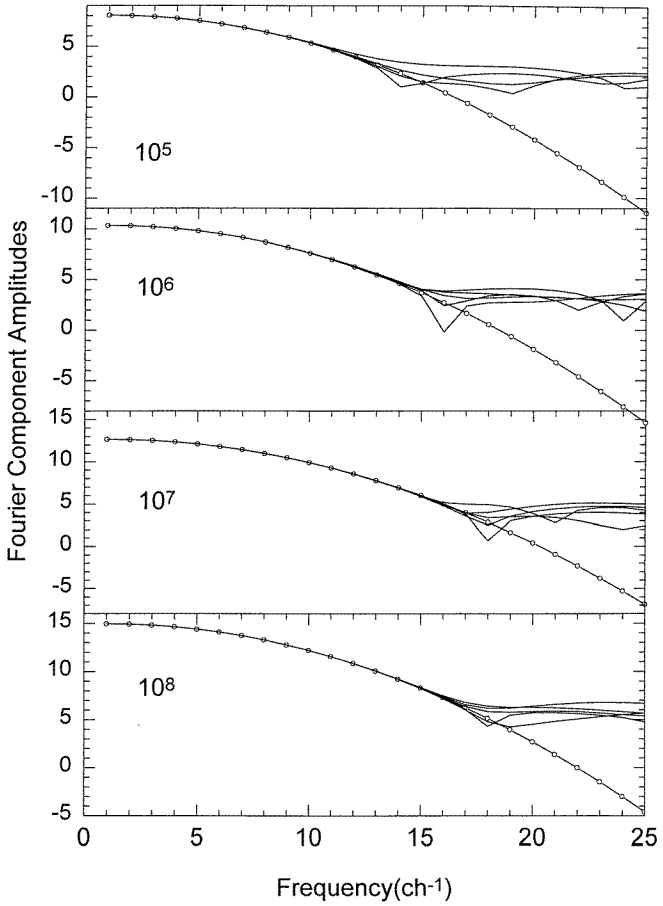

Figure 6. Comparison of Fourier amplitude spectra of perfect Gaussian (open circles) and Monte Carlo generated Gaussian shaped HIFs for number of spectral events N_{cts} equal to 10^5, 10^6, 10^7 and 10^8. It may be seen that as N_{cts} increases so does the frequency ν_0 at which departure occurs from the correct coefficient.

An important consideration is the range of spatial visualization in an experimental AF plot. If it is insufficient then much important structural detail of the defect will be missing. In figure 8 we show schematically the close connection that exists between Stokes' deconvolution method and the construction of the one dimensional AF map $B^{2\gamma}(z)$ from (ACAR or DBAR) $N(p_z)$ spectra. It can be seen that since on the stokes method one divides the FT[$N(p_z)$] by the FT[HIF(p_z)] to obtain $B^{2\gamma}(z)$ (which is seen as the inverse Fourier transform of the deconvoluted $N(p_z)$), the cut-off frequency ν_0 determines the extent of visualization in z space. Under discrete Fourier transformation the discretizations in z space

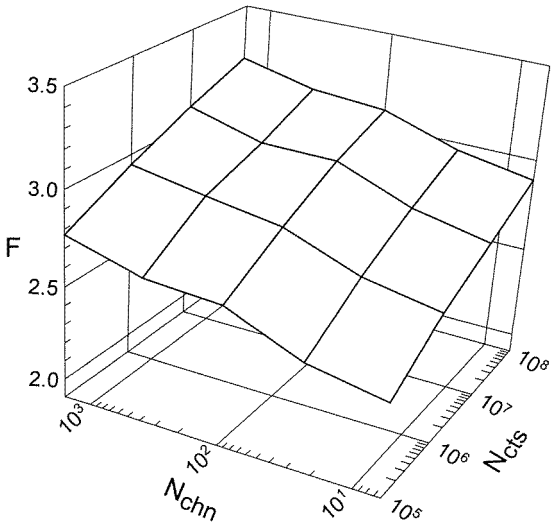

Figure 7. The deconvolution improvement factor, F, plotted against N_{cts}, the number of spectrum counts, and N_{chn}, the number of discrete spectral bins across the fwhm of the HIF.

will be of width $K^{-1}(=\frac{1}{2}\overline{h}cE^{-1})$ so that the range r_{max} is given by:

$$r_{max} = \nu_0 K^{-1} \approx 0.603\frac{\overline{h}c}{\text{fwhm(RIF)}}. \tag{21}$$

Taking an fwhm(RIF) of 230 eV, as estimated above, one obtains $r_{max} = 5.2$ Å (10 au). Improved deconvolution techniques [31, 35–37], which in Fourier space do not truncate abruptly [32], will undoubtedly extend this range estimate to some extent. Equation (21) is written for D-DBAR in energy units, but may similarly be applied to raw ACAR spectra which can achieve resolutions ∼0.5 mrad (127 eV). It is thus expected that ACAR should readily produce $B^{2\gamma}(x, y)$ visualizations to 20 au. Recent confirmation of this has come from the work of LiMing *et al* [11] who, working with the 0.5 mrad resolution 1D-ACAR data of Shulman *et al* [28] were able to see the expected oscillatory behaviour in $B^{2\gamma}(z)$ out to this range. The indications are then, based on the theoretical $B^{2\gamma}(x, y)$ plots of section 3, that D-DBAR and to a greater extent ACAR data should be able to show important defect structural detail. For example, as suggested in section 3, one might hope to see out to the distance where there is zero wavefunction product autocorrelation due to the positron wavefunction localization at a vacancy defect. Such observation would allow an unequivocal decision on whether the positron state was that of a vacancy, or whether any measurable fraction of positrons were annihilating from the bulk Bloch states.

One of the useful aspects of dealing with the autocorrelation is the helpful way in which it encodes all the information in the 1D momentum distribution $N(p_z)$ into a single line in $B^{2\gamma}(\boldsymbol{r})$ space [15].

$$B^{2\gamma}(z) = \frac{1}{\sqrt{2\pi}}\int_{-\infty}^{+\infty} N(p_z)\,\mathrm{e}^{\mathrm{i}k_z z}\,\mathrm{d}k_z. \tag{22}$$

This fact has been widely exploited in $\rho^{2\gamma}(\boldsymbol{p})$ 3D momentum reconstructions [20]. Here the form of equation (22) suggests the idea of rotating the sample about a certain crystal axis (e.g. by using a stepper motor) and for each 2γ annihilation event recording the angle

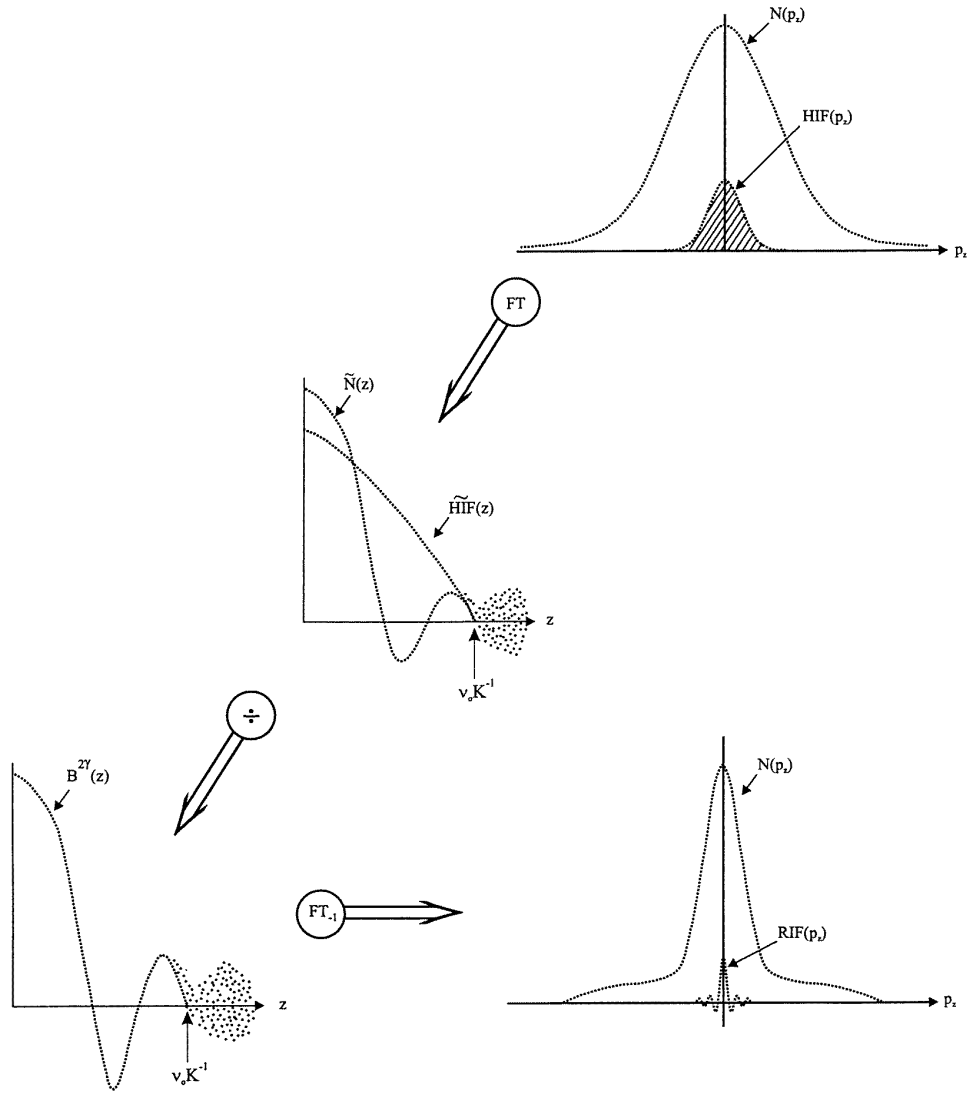

Figure 8. Schematic showing the close interconnection between the process of Stokes deconvolution and production of the 1D-AF plot. The maximum range is given by the cut-off frequency in Fourier (real) space as described in the text.

of the sample (e.g. by counting motor pulsings). Events could then be 'binned' according to angle and the autocorrelation function $B^{2\gamma}(r, \bar{\theta})$ for mean bin angle $\bar{\theta}$ formed by Fourier transformation plus filtering as already outlined. The thus-formed $B^{2\gamma}(r, \bar{\theta})$ may then be used for defect identification, although if desired it could always be Fourier transformed back to form what might truly be referred to as 2D DBAR spectroscopy (it being the direct analogue of 2D-ACAR). One advantage of 2D-DBAR over 2D-ACAR would be the fact that it would not require a high source activity, but a disadvantage is that the two Ge detectors, due to their proximity to the sample and wide solid-angle subtendence, convolute a fairly

wide range of directions [40]. This could only be improved by moving the detectors back from the sample, which would in turn require more positrons annihilating per second at the target. In comparing theory with experiment, however, integration could be performed over the theoretical $B^{2\gamma}(r, \bar{\theta})$ both to incorporate the solid-angle effect and the effect of finite angular bin size.

5. Conclusions

At the present time it is clear that defect AFs could, if obtained either experimentally or theoretically, form a library from which defects may be identified. What is not however clear at present is just how much structural information arising from annihilation with localized defect electron orbitals may be obtained from direct observation of experimental AF mappings. The uncertainty stems mainly from the fact that the annihilation radiation from a defect is not exclusively from the localized electron orbitals. A significant fraction appears to come from delocalized valence states. Whether these delocalized states themselves contain important structural information, for example in the form of phase shifts arising from the perturbation imposed by the defect, is another consideration needing further thought and clarification.

One thing that can be stated with some certainty, however, is that the AF visualization range is very important, seeing that this permits an inspection of the diffraction detail. We have shown that the visualization range is inversely related to the instrumental resolution function. For very high resolution ACAR (or possibly D-DBAR) spectroscopy the visualization range could be sufficiently large so as to make a clear distinction between a defect AF plot, which decays to zero intensity at some range commensurate with the spread of the positron wavefunction, and the bulk crystal Bloch state AF plot which continues to ripple along the Bravais lattice. Such plots may make for a higher confidence level in distinguishing between saturation and zero positron trapping regimes.

Another advantage of working with AF plots is that, unlike the presentation of the defect diffraction information in the form of a 2D-ACAR spectrum where all the information is compressed close to the centre of the plot on top of the momentum 'hill', the structural information is spread out towards the outer regions of the plot, making for easier visualization and interpretation. Coupled to this is the fact that the plot will be in real-space coordinates, and thus more tangible to the spectroscopist, who could, for example, overlap the plot with the known (unrelaxed) atomic lattice positions. Moreover, the conventional *S* and *W* information obtained in momentum spectroscopy would not be lost in the process of Fourier inversion, and defined radii on the AF plot would correspond to the 'core' region and the 'valence' region. Indeed the operation of forming these parametrizations may be clearer in an AF plot as the mean core orbital radii are known.

Much of the above is still speculation. The next step is clearly to take both experimental 2D-ACAR and 2D-DBAR spectra and form AF mappings of known defects. In terms of D-DBAR it will be important to put effort into checking results of the present work with regard to the achievable RIF resolutions. The need for further theoretical work is also clearly indicated, in particular the determination of the relative contributions of localized defect orbitals and delocalized valence orbitals.

Acknowledgments

Y L Luo and K C Yip are thanked for their help in preparation of this manuscript.

References

[1] See for example the reviews Schultz P J and Lynn K G 1987 *Rev. Mod. Phys.* **60** 701
Puska M J and Nieminen R M 1994 *Rev. Mod. Phys.* **66** 841

[2] See for example MacKensie I K 1983 *Positron Solid State Physics, Proc. Int. School Phys. 'Enrico Fermi' Course 83* ed W Brandt and A Dupasquier (IOS Press) p 196

[3] Liszkay L, Corbel C, Baroux L, Hautojärvi P, Bayhan M, Brinkman A W and Tararenko S 1994 *Appl. Phys. Lett.* **64** 380

[4] Alatalo M, Kauppinen H, Saarinen K, Puska M J, Mäkinen J, Hautojärvi P and Nieminen R M 1995 *Phys. Rev.* B **51** 4176

[5] Fluss J M, Berko S, Chakraborty B, Lippel P and Siegel R W 1984 *J. Phys. F: Met. Phys.* **14** 2855

[6] See for example Puska M J and Nieminen R M 1994 *Rev. Mod. Phys.* **66** 841
West R N 1995 *Positron Spectroscopy of Solids, Proc. Int. School Phys. 'Enrico Fermi' Course 125* ed A Dupasquier and A P Mills Jr (IOS Press) p 75

[7] Peng J P, Lynn K G, Umlor M T, Keeble D J and Harshman D R 1994 *Phys. Rev.* B **50** 11 247

[8] Ambigapathy R, Manuel A A, Hautojärvi P, Saarinen K and Corbel C 1994 *Phys. Rev.* B **50** 2188

[9] McMullen T and Bishop M F 1997 *Phys. Rev.* B **55** 4046

[10] Berko S 1983 *Positron Solid State Physics, Proc. Int. School Phys. 'Enrico Fermi' Course 83* (IOS Press) p 76

[11] LiMing W, Panda B K, Fung S and Beling C D 1997 *J. Phys.: Condens. Matter* **9** 8147

[12] Panda B K, LiMing W, Fung S and Beling C D 1997 *Phys. Rev.* B **56** 7356

[13] Asoka-Kumar P, Alatalo M, Ghosh V J, Kruseman A C, Nielsen B and Lynn K G 1996 *Phys. Rev. Lett.* **77** 2097

[14] Lynn K G and Goland A N 1976 *Solid State Commun.* **18** 1549
Lynn K G, MacDonald J R, Boie R A, Feldman L C, Gabbe J D, Robbins M F, Bonderup E and Golovchenko J 1977 *Phys. Rev. Lett.* **38** 241

[15] Britton D T, Junker W and Sperr P 1992 *Mater. Sci. Forum* **105–110** 1845

[16] Bourgoin J and Lannoo M 1983 *Point Defects in Semiconductors II (Springer Series in Solid-State Science)* (Berlin: Springer) ch 2

[17] Beling C D, Fung S, Au H L, Ling C C, Reddy C V, Deng A H and Panda B K 1997 *Appl. Surf. Sci.* **116** 121

[18] See for example Champeney D C 1973 *Fourier Transforms and their Physical Applications* (London: Academic) p 73

[19] Mueller F M 1977 *Phys. Rev.* B **15** 3039

[20] Pecora L M 1989 *J. Phys.: Condens. Matter* **1** SA1

[21] Schülke W 1977 *Phys. Status Solidi* b **82** 229

[22] Stumpf R and Scheffler M 1994 *Comput. Phys. Commun.* **79** 447

[23] Bachelet G B, Hamann D R and Schlüter M 1982 *Phys. Rev.* B **26** 4199

[24] Kleinman L and Bylander D M 1982 *Phys. Rev. Lett.* **48** 1425

[25] Chadi D J and Cohen M L 1973 *Phys. Rev.* B **8** 5747

[26] Boronski E and Nieminen R M 1986 *Phys. Rev.* B **34** 3820

[27] Panda B K 1992 *Phys. Status Solidi* b **170** 481

[28] Shulman M A, Beardsley G M and Berko S 1975 *Appl. Phys.* **5** 367

[29] Performance of digital signal processors for gamma spectrometry 1997 *Canberra Applications Note*

[30] Shizuma K 1978 *Nucl. Instrum. Methods* **150** 447

[31] Britton D T, Bentvelsen P, DeVries J and Van Veen A 1988 *Nucl. Instrum. Methods Phys. Res.* A **273** 343

[32] Paatero P, Manninen S and Paakkari T 1974 *University of Helsinki Report Series in Physics* 75

[33] Cheung S H, Beling C D, Fung S and Mackeown M K 1997 *Mater. Sci. Forum* **255–257** 738

[34] Stokes A R 1948 *Proc. Phys. Soc.* **61** 382

[35] Panda B K, Fleischer S, Ling C C, Beling C D, Fung S and Panda S 1995 *Appl. Surf. Sci.* **85** 182

[36] Kong Y and Lynn K G 1991 *Nucl. Instrum. Methods* A **302** 145

[37] Calderin L and Diaz J J 1996 *Nucl. Instrum. Methods Phys. Res.* B **117** 457

[38] Lynn K G 1998 private communication

[39] Hara T and Schaffer J P 1988 *J. Phys. E: Sci. Instrum.* **21** 595

[40] Mijnarends P E, Kruseman A C, van Veen A, Ghosh V J, Asoka-Kumar P, Bansil A, Kaprzk S and Lynn K G 1997 *Mater. Sci. Forum* **255–257** 784